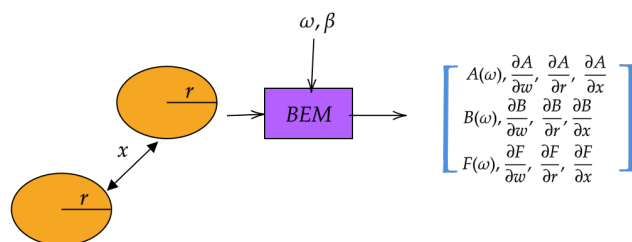


Graphical Abstract

Fully Differentiable Boundary Element Solver for Hydrodynamic Sensitivity Analysis of Wave-Structure InteractionsKapil Khanal^a, Carlos A. Michelén Strófer^b, Matthieu Ancellin^c, Maha Haji^a

Highlights

Fully Differentiable Boundary Element Solver for Hydrodynamic Sensitivity Analysis of Wave-Structure Interactions

Kapil Khanal^a, Carlos A. Michelén Ströfer^b, Matthieu Ancellin^c, Maha Haji^a

- Novel differentiable BEM solver computes exact gradients for hydrodynamic analysis.
- Supports exact and surrogate Green's functions for efficiency and accuracy trade-offs.
- Derivation of discrete adjoint method for BIE to enable scalable sensitivity analysis.
- Validated against benchmarks and applied to WEC design optimization with AD.
- Enables efficient integration into MDO frameworks for offshore energy systems design.

Fully Differentiable Boundary Element Solver for Hydrodynamic Sensitivity Analysis of Wave-Structure Interactions

Kapil Khanal^a, Carlos A. Michelén Ströfer^b, Matthieu Ancellin^c, Maha Haji^a

^a*Cornell University, Ithaca, 14850, NY, USA*

^b*Sandia National Laboratories, Albuquerque, 87123, NM, USA*

^c*Eurobios Mews Labs, Paris, France*

Abstract

Accurately predicting wave-structure interactions is critical for the effective design and analysis of marine structures. This is typically achieved using solvers that employ the boundary element method (BEM), which relies on linear potential flow theory. Precise estimation of the sensitivity of these interactions is equally important for system-level applications such as design optimization. Current BEM solvers are unable to provide these sensitivities as they are not differentiable. To address these challenges, we have developed a fully-differentiable BEM solver for marine hydrodynamics, capable of calculating diffraction and radiation coefficients, and their derivatives with high accuracy. This new solver implements both direct and indirect BEM formulations and incorporates two Green's function expressions, offering a trade-off between accuracy and computational speed. Gradients are computed using reverse-mode automatic differentiation (AD) within the Julia programming language. As a first case study, we analyze two identical floating spheres, evaluating gradients with respect to physical dimensions, inter-sphere distance, and wave frequency. Validation studies demonstrate excellent agreement between AD-computed gradients and finite-difference results. In a second case study, we leverage AD-computed gradients to optimize the mechanical power production of a pair of wave energy converters (WECs). This represents the first application of gradients in WEC power optimization, offering valuable insights into hydrodynamic interactions and advancing the understanding of layout optimization for maximum efficiency. Beyond power optimization, the differentiable BEM solver highlights the potential of AD for offshore design

studies. It paves the way for broader applications in machine learning integration, optimal control, and uncertainty quantification of hydrodynamic coefficients, offering new directions for advancing wave-structure interaction analysis and system-level optimization.

Keywords: Differentiable solver, Boundary element code, Adjoint, Exact Sensitivities

1. Introduction

The determination of the wave-induced response of an offshore structure depends on its hydrodynamic coefficients. These coefficients are determined by considering both the wave diffraction problem (how waves are scattered by a stationary structure) and the wave radiation problem (how waves are generated by the motion of the structure itself). Several methods exist to solve both the wave diffraction and radiation problems, including analytical approaches [25], surrogate models [66], and numerical solvers [3, 36, 5]. Analytical and surrogate models, however, are often limited in their applicability due to geometrical assumptions (e.g., axisymmetry of a structure), modeling methods (e.g., a solution being comprised of certain basis functions) or rely on pre-trained data (e.g., in the case of surrogate models). Consequently, numerical solvers remain the preferred choice for general hydrodynamics problems due to their flexibility and accuracy across diverse geometries.

Numerical hydrodynamic solvers generally utilize the boundary element method (BEM) which focuses on the boundaries of the domain rather than the entire volume, thereby significantly reducing computational effort while maintaining the accuracy. This approach transforms the governing partial differential equations (PDEs) into boundary integral equations (BIEs), making it particularly effective for problems with infinite or semi-infinite domains as is the case for analyzing the hydrodynamic forces on offshore bodies. Mature BEM solvers [3, 5, 32, 36] are used for the design and analysis of large offshore structures such as, offshore wind turbines [4], and wave energy converters (WECs) [59].

Recent advancements in computational methods highlight the importance of sensitivity analysis in engineering design [39]. Sensitivity analysis elucidates how variations in input parameters influence model outputs, enabling optimization, uncertainty quantification, and robust design. Automatic dif-

ferentiation (AD)—a computational technique for exact gradient calculation using differentiation by a computer program—has emerged as a transformative tool in this context [6]. Unlike finite difference methods, AD computes derivatives analytically, ensuring high accuracy and computational efficiency. This technique has been successfully applied in fields such as design optimization [40], machine learning [51], optimal control [21], inverse problems [60], and uncertainty quantification using adjoint-based formulations [7]. In computational fluid dynamics (CFD), for example, AD has enabled the development of gradient-based optimization algorithms that significantly improve the design of aerodynamic and hydrodynamic systems [29, 61]. In optimal control, AD has facilitated the precise calculation of control sensitivities, enhancing the performance of control systems in applications ranging from aerospace to robotics [21].

However, these AD-enabled advancements are yet to be widely adopted in marine hydrodynamics. Unlike domains such as acoustics [58, 54], structures [24] and electromagnetics [30], where BEM solvers integrate gradient computations, the mathematical complexity of marine-specific kernel—such as the free surface Green’s function—has hindered progress [44]. Despite their strengths, existing BEM solvers lack the capability to compute gradients directly—a critical limitation for optimization and sensitivity analysis. They lack this capability as they are not designed to propagate the sensitivities of input and outputs. For optimization studies, BEM solvers have therefore been coupled with statistical [57] or heuristic [59] methods that do not require gradients, or gradient-based methods relying on finite differences for gradient computation. While effective for small-scale problems, these approaches are computationally expensive and impractical for large systems such as those with a significant number of bodies, requiring numerous gradient evaluations. While gradients can be directly efficiently and accurately computed in the case of analytical and surrogate model hydrodynamic analysis methods, analytical methods are constrained by simplifying assumptions, while surrogate models, despite balancing efficiency and accuracy, suffer from limited applicability outside their training domains [16].

The lack of accurate and efficient gradients from BEM solvers restricts system-level applications, where scalable methods are essential for analyzing subsystems in one coupled model. Multidisciplinary Design Optimization (MDO), a framework that integrates and optimizes across multiple interacting disciplines or subsystems simultaneously, has shown promise in addressing this challenge. Recent studies underscore the advantages of incorporating

gradients into MDO frameworks for offshore floating structures [47]. For example, analytical gradient derivations for substructures of offshore floating wind turbines have been integrated with broader analysis, advancing practical engineering capabilities [12]. Gradients also offer new opportunities for the development of marine renewable energy systems, as emphasized in the U.S. DOE “Next Generation Marine Energy Software Needs Assessment” report [50], and hold potential for accelerating machine learning-based marine hydrodynamic innovations [67].

To overcome the limitations of existing BEM solvers in computing accurate and efficient gradients, this paper introduces a novel differentiable BEM solver implemented in Julia. This new solver computes accurate hydrodynamic coefficients and their exact gradients with respect to the wave environment, physical dimensions, and degree of freedom using exact and surrogate Green’s functions via direct and indirect boundary integral formulations. This solver has the capability to enable detailed sensitivity analyses and integrate seamlessly into optimization workflows, thereby accelerating the design of offshore structures such as WECs and floating wind turbine substructures. The solver also accommodates various approximations of Green’s functions, giving it flexibility in balancing accuracy and computational cost across different design stages [2].

The remainder of this paper is organized as follows. In Section 2, we discuss the mathematical formulation of the new BEM solver. Following in Section 3 we discuss the solver’s adjoint-based differentiation approach. We detail the solver’s implementation Julia in Section 4. In Section 5 we validate the solver’s ability to compute accurate gradients for the case of two identical spheres with respect to their radius, the distance between them, and the incident wave frequency. Finally, in Section 6 we demonstrate the ability of the solver to be used in gradient-based optimization of mechanical power for a pair of identical WECs before concluding in Section 7 and outlining avenues for future work in Section 8.

2. Hydrodynamic Formulation and Numerical Approach

Assuming the fluid flow around the floating body, as illustrated in Figure 1, is incompressible ($\nabla \cdot \mathbf{v} = 0$), irrotational ($\nabla \times \mathbf{v} = 0$), and inviscid, the velocity vector, \mathbf{v} , can be written as the gradient of a velocity potential function, $\phi(x, y, z)$:

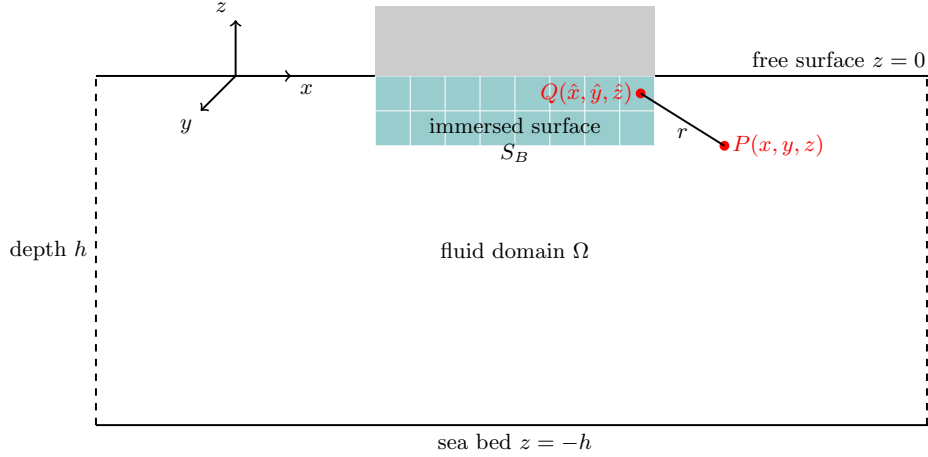


Figure 1: Fluid domain in three dimensions with source point P and field point Q .

$$\mathbf{v} = \nabla\phi. \quad (1)$$

$\phi(x, y, z)$ can be further decomposed into three parts: the incident wave potential $\phi_0(x, y, z)$, the diffracted wave potential $\phi_d(x, y, z)$, and the radiated wave potential $\phi_r(x, y, z)$:

$$\phi = \phi_0 + \phi_d + \phi_r. \quad (2)$$

ϕ satisfies the Laplace equation

$$\nabla^2\phi = 0 \quad (3)$$

subject to boundary conditions on the free surface, sea bottom, on the body surface, and in the far field.

The boundary condition on the free surface is linearized under the assumption of small wave amplitudes and small motion of the floating body. In the case of deep-water waves, where the influence of the sea floor on wave particle trajectories is negligible, the solution to the Laplace equation that satisfies the specified boundary conditions is sinusoidal [14]. This characteristic enables the separation of the velocity potential into temporal and spatial components [15]. Hence, this fully linear problem can then be examined in the frequency domain using the complex-valued phasor Φ :

$$\phi = \Re(\Phi e^{i\omega t}) \quad (4)$$

where \Re denotes the real part, ω is the frequency of the incident wave in rad/s, and t is time.

The boundary conditions then become:

1. Linearized free surface continuity at $z = 0$:

$$g \frac{\partial \Phi}{\partial z} = \omega^2 \Phi. \quad (5)$$

2. Zero-flux at the sea bed at $z = -h$:

$$\frac{\partial \Phi}{\partial z} = 0. \quad (6)$$

3. On the immersed body surface S_b
 - (a) for the radiation problem:

$$\nabla \phi_r \cdot \mathbf{n} = \mathbf{u} \cdot \mathbf{n} \quad (7)$$

- (b) for the diffraction problem:

$$\nabla \phi_d \cdot \mathbf{n} = -\nabla \Phi_0 \cdot \mathbf{n} \quad (8)$$

where z is the vertical distance from the free surface (z -axis positive upward), g is the gravitational constant, h represents the ocean depth, \mathbf{n} is the normal vector at the surface of the floating body pointing outward, \mathbf{u} is the velocity of the floating body, and Φ_0 is the complex-valued phasor associated with the incident potential, ϕ_0 , in the same manner as described by Eq. (4) for the full potential ϕ .

Additionally, ϕ must satisfy the Sommerfield radiation condition at the far-field boundary ($r \rightarrow \infty$) which shows that the velocity potential gradually decays with the horizontal distance and eventually vanishes in the far field:

$$\lim_{kr \rightarrow \infty} r^{1/2} \left(\frac{\partial \phi}{\partial r} - ik\phi \right) = 0. \quad (9)$$

where r denotes the horizontal distance from the body and k is the wavenumber.

Once Eq. (3) has been solved with the associated boundary conditions, the potential on the body can be used to derive the pressure and thus the force between the water and floating body.

To solve the Laplace Eq. (3) efficiently using BEM, the problem is reformulated as a BIE. Following [2], two primary methods for this transformation are discussed and summarized in the following sections: the direct and indirect BIE. Reference textbooks on this topic include [52] and [17].

2.1. Direct boundary integral equations

The direct BIE, often referred to as the “potential” or “sources-and-dipoles” formulation, is widely used in existing BEM solvers WAMIT [32] and HAMS [36]. Denoting the immersed boundary of the body as S_B , the BIE reads

$$\frac{\Phi(x)}{2} + \iint_{S_B} \Phi(\xi) \nabla_2 G(x, \xi) \cdot n(\xi) d\xi = \iint_{S_B} \frac{\partial \Phi}{\partial n}(\xi) G(x, \xi) d\xi \quad \forall x \in S_B \quad (10)$$

where $G(x, \xi)$ is the fundamental solution (the Green’s function) of the problem, n is the normal vector, and ∇_2 indicates the gradient with respect to the second variable in Green’s function, ξ in this case. Using a collocation method and discretizing the boundary into N panels, the equation becomes:

$$D\Phi = S \frac{\partial \Phi}{\partial n} \quad (11)$$

where the matrix S , sometimes called single-layer operator, is defined as

$$S_{ij} = \iint_{S_{B_j}} G(x_i, \xi) d\xi \quad (12)$$

and the D matrix, sometimes referred to as the double-layer operator, is defined as

$$D_{ij} = \frac{\delta_{ij}}{2} + \iint_{S_{B_j}} \nabla_2 G(x_i, \xi) \cdot n_j d\xi \quad (13)$$

where δ_{ij} is the Kronecker delta and n_j denotes the normal vector of panel S_{B_j} .

2.2. Indirect boundary integral equations

The indirect BIE, also known as the “sources” formulation, introduces a new scalar field, σ defined on S_B . The equations for $\Phi(x)$ are formulated as:

$$\Phi(x) = \iint_{S_B} \sigma(\xi) G(x, \xi) d\xi \quad \forall x \in S_B \quad (14)$$

and

$$\frac{\partial \Phi}{\partial n}(x) = \frac{\sigma}{2} + \iint_{S_B} \sigma(\xi) \nabla_1 G(x, \xi) \cdot n(x) d\xi \quad \forall x \in S_B \quad (15)$$

where ∇_1 denotes the gradient taken with respect to the first variable (x in this case).

After discretization as in the direct BIE, these equations are expressed as:

$$\Phi = S\sigma \quad (16)$$

and

$$\frac{\partial \Phi}{\partial n} = K\sigma \quad (17)$$

where K is the adjoint double-layer operator defined as

$$K_{ij} = \frac{\delta_{ij}}{2} + \iint_{S_{B_i}} \nabla_1 G(x_i, x_i) \cdot n_i d\xi \quad (18)$$

where n_i denotes the normal vector of panel S_{B_i} .

2.3. Relationship Between Double-Layer Operators

The relationship between the gradients $\nabla_1 G$ and $\nabla_2 G$ is derived from the symmetry property of the Green's function:

$$G(x, \xi) = G(\xi, x). \quad (19)$$

Differentiating with respect to ξ , we have:

$$\nabla_2 G(x, \xi) = \nabla_1 G(\xi, x). \quad (20)$$

This symmetry allows for efficient computation of D and K using shared code, with minor adjustments for switching between symmetric and antisymmetric components.

The new solver described in this paper integrates multiple capabilities for hydrodynamic coefficient calculation including both direction and indirect BIE formulations. It is compared against other open-source solvers and their capabilities in Table 1.

Solver	Green's Function Evaluation Method		BIE Formulation	Irregular Frequencies Removal	Parallelization	Differentiable
	Wu et al. (2017) [63]	Delhommeau (1987) [11]				
This solver v0.1.0	Yes	Yes	Direct & Indirect	No	No	Yes
Capytaine v2.2.1 [3]	No	Yes	Direct & Indirect	Yes	Yes	No
HAMS [36]	Yes	No	Direct only	Yes	Yes	No

Table 1: Comparison of open-source solvers based on their capabilities.

2.4. Evaluation of the Green's function

Numerous approaches have been explored in the literature to formulate and compute the Green's function for the linear potential flow problem [64]. Developing computationally efficient approximations for the Green's function and its gradients remains an active area and evolving field of research, as highlighted in studies such as [64, 38, 28].

Newman (1985) outlines efficient numerical algorithms for evaluating the free-surface Green's function and its derivatives for linearized three-dimensional wave motions, considering both infinite and constant finite fluid depths [44, 45]. By leveraging series expansions and multi-dimensional polynomial approximations, Newman's methods significantly enhance the computational efficiency of Green's function calculations compared to traditional numerical integration techniques. These polynomial approximation replace the exact computations, which are often difficult to evaluate and differentiate with the required level of accuracy [34]. Other approximations of the Green's function utilize computational domain decomposition, such as the six domain approach in Newman's method [32], and apply specialized techniques like Legendre or double Chebyshev polynomial approximations for different ranges [64].

In this paper, we develop a new BEM solver that allows users to choose between either an exact expression for the Green's function derived by Delhommeau (1987) [11] or a recently derived global approximation developed by Wu et al. (2017) [63]. The exact expression implementation is significantly slower but is highly accurate and is included for verification and validation. Though we only discuss one approximation for the Green's function in the implementation presented here, the software architecture of the new solver described in this paper enables seamless integration of any Green's function formulation, allowing users to compute hydrodynamic coefficients and their gradients efficiently. This flexibility supports design optimization workflows, permitting the use of faster Green's function approximations during early-stage design studies and transitioning to more precise but computationally

intensive options for late-stage analyses, all within the same software framework.

The remainder of this section will focus on the implementation of the approximation of the Green’s function derived by Wu et al. (2017) [63]. This Green’s function approximation is accurate enough for the determination of accurate hydrodynamic coefficients, and hence sufficient for design optimization studies [35].

In this formulation, the Green’s function, G , is written as

$$4\pi G = -\frac{1}{\mathcal{R}} + L + W \quad (21)$$

where R represents the Euclidean distance between the source point $P(x, y, z \leq 0)$ and field point $Q(\bar{x}, \bar{y}, \bar{z} \leq 0)$, and L and W account for non-oscillatory local flow and pulsating surface waves on the free surface components, respectively. The first term in Equation (21), $-\frac{1}{\mathcal{R}}$, is often referred to as the “Rankine” term. All coordinates are non-dimensional with respect to the wavenumber (k).

The wave component W can be expressed as:

$$W(h, v) = 2\pi [H_0(h) + iJ_0(h)] e^v \quad (22)$$

where $H_0(h)$ and $J_0(h)$ are the zeroth-order Struve and Bessel functions, respectively, $h = \sqrt{(x - \bar{x})^2 + (y - \bar{y})^2}$ is the horizontal distance and $v = (z + \bar{z}) \leq 0$ is the vertical distance (from the free surface) between the panels. The approximation for $H_0(h)$ and $Y_0(h)$ are detailed in Newman (1984) [43].

The local flow component L is approximated as:

$$L \approx \frac{-1}{d} + \frac{2\mathcal{P}}{1 + d^3} + L' \quad (23)$$

where

$$\mathcal{P} \equiv e^v \left(\log \frac{d - v}{2} + \gamma - 2d^2 \right) + d^2 - v \quad (24)$$

and

$$L' \approx (\rho(1 - \rho)^3(1 - \beta))A(\rho) - \beta B(\rho) - \frac{\alpha C(\rho)}{1 + 6\alpha\rho(1 - \rho)} + \beta(1 - \beta)D(\rho) \quad (25)$$

where $d = \sqrt{h^2 + v^2}$, $\rho = \frac{d}{1+d}$, $\beta = \frac{h}{d}$, γ is Euler’s constant, and $A(\rho)$, $B(\rho)$, $C(\rho)$, and $D(\rho)$ are 9th-order polynomials in ρ with coefficients specified

in Wu et al. (2017) [63]. The first term in (23), $\frac{1}{d}$, is often referred to as the “reflected Rankine” term. Wu et al. (2017) [63] similarly derive an approximation for local flow component (L^*) and the wave component (W_h) for $\nabla G = [G_x, G_y, G_z]$.

This global approximation replaces the challenging integral computation of L with polynomial approximations, significantly simplifying numerical implementations. The parameters $R, h, v, d, \nu, H_0, Y_0$, and γ define the computational domain and characterize the interactions between the source point P and the field point Q . In BEM codes, the computational flow domain is primarily determined by h and v , representing the horizontal and vertical distances between the panels P and Q relative to the free surface.

Unlike other methods, discussed in Xie et al (2018) [64], that subdivide the flow domain into multiple subdomains, requiring extensive tabulation and interpolation, the method detailed by Wu et al. (2017) [63] utilizes elementary functions defined consistently across the entire domain. This not only avoids the additional computational overhead but also ensures that the solution and its derivatives are easily accessible. From a numerical perspective, this method is well-suited for AD due to its inherent simplicity and efficiency. Both forward and backward passes can be parallelized, making this approach computationally efficient and straightforward to implement.

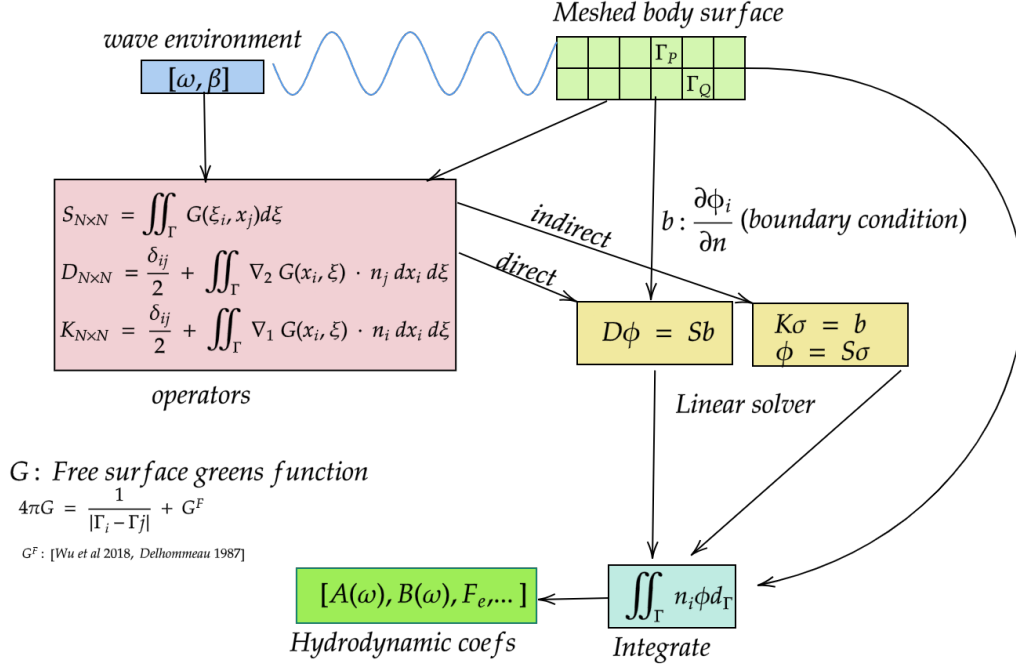


Figure 2: Julia implementation of BEM software

Figure 2 summarizes the architecture of the new solver described in this paper and its various operations. This new solver calculates the influence matrices (operators) S and D or K for a floating body discretized into flat panels. The choice of direct BEM and indirect BEM and the choice of the Green's function calculates the potentials and the hydrodynamic forces with varying accuracy and efficiency.

2.5. Validation of hydrodynamic coefficients and excitation forces

In this section, we present the validation results of our new solver for computing hydrodynamic coefficients and wave excitation forces, which are critical for the design and analysis of offshore structures and floating bodies. Having determined the velocity potentials, the corresponding hydrodynamic pressure is obtained by the linearized Bernoulli's equation:

$$P = -\rho_w \frac{\partial \phi}{\partial t} \quad (26)$$

where ρ_w is the density of water. Integrating the potential on the wetted surface of the floating body and separating the result into real and complex parts yields the added mass, A_{ij} and damping B_{ij} hydrodynamic coefficients:

$$\omega^2 A_{ij} - i B_{ij} \omega = \rho_w \iint_{S_B} n_i \phi_j dS. \quad (27)$$

As will be shown later, $A_{ij}(\omega)$ and $B_{ij}(\omega)$ make up the radiation force. The added mass is the mass of the fluid that accelerates with the body, while radiation damping is the reciprocal force the fluid exerts on the body.

To evaluate the accuracy of the new solver's computation of the added mass and damping coefficients, we compare its results with the analytical solutions for a submerged unit hemisphere's added mass and damping coefficients, as presented in [25]. The comparison, detailed in Figures 3 and 4 for the heave and surge coefficients, respectively, shows good agreement between the new solver developed in this work and the analytical solutions. The discrepancy in the surge coefficients compared to Wu et al.'s [63] validation is likely due to the use of a simpler integration method (one point approximation) over the panels. Future work will address this by incorporating more accurate and differentiable integration or quadrature methods.

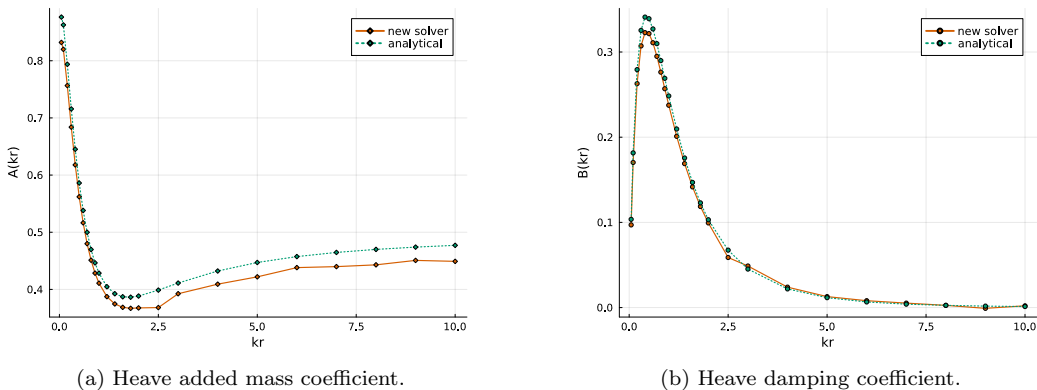


Figure 3: Comparison of the heave hydrodynamic coefficients for (a) added mass and (b) damping, as computed by the new solver, with analytical results for a submerged unit hemisphere from [25].

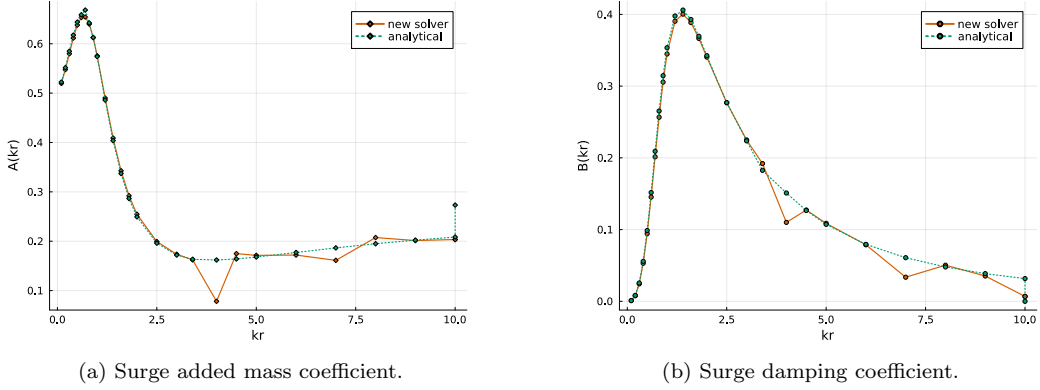


Figure 4: Comparison of surge hydrodynamic coefficients for (a) added mass and (b) damping, as computed by the new solver, with and analytical results for a submerged unit hemisphere from [25].

Similarly, we compute the wave excitation forces, F_i , for validation purposes. This can be determined either from the Haskind relations:

$$F_i = -i\omega\rho_w \iint_{S_B} \left(n_i\phi_0 - \phi_i \frac{\partial\phi_i}{\partial n} \right) dS \quad (28)$$

or from direct integration of the hydrodynamic pressure:

$$F_i = - \iint_{S_B} p \mathbf{n} dS \quad (29)$$

where the subscript $i = 1, \dots, 6$ denotes the degree of freedom. The total wave excitation force is the sum of the Froude-Krylov force due to the pressure field of the undisturbed incident wave, F_{FK} , and diffraction forces, F_D :

$$F_i = F_{FK} + F_D. \quad (30)$$

The Froude-Krylov force can be determined from the integration of the incident wave field pressure as

$$F_{FK} = \rho_w \iint_{S_B} \frac{\partial\phi_0}{\partial t} \mathbf{n} dS. \quad (31)$$

While the diffraction force can be determined from the integration of the diffracted wavefield pressure as

$$F_D = \rho_w \iint_{S_B} \frac{\partial \phi_d}{\partial t} \mathbf{n} dS. \quad (32)$$

Additionally, the radiation force, F_R , can be easily obtained from the added mass and damping coefficients determined previously:

$$F_R = \rho \iint_{S_B} \frac{\partial \phi_r}{\partial t} \mathbf{n} dS = A_{ij} \dot{u}_j + B_{ij} u_j \quad (33)$$

where u_j is the j -th component of the body velocity, \mathbf{u} and \dot{u}_j is its time-derivative (aka acceleration).

Figure 5 presents the comparison of the new solver for Froude-Krylov and diffraction forces for a submerged unit hemisphere with those being obtained using the exact expression for the Green's function derived by Delhommeau (1987) [11] as implemented in the popular BEM software Capytaine [3]. This comparison highlights the solver's accuracy in calculating wave excitation forces, a critical component for assessing wave-structure interactions.

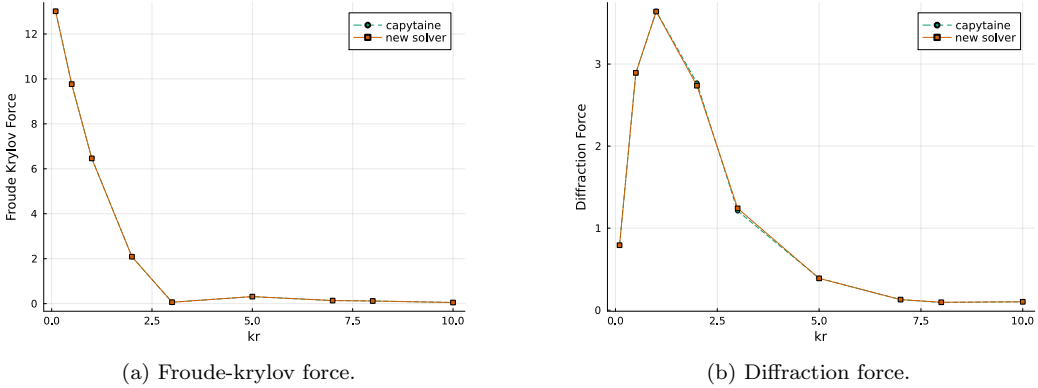


Figure 5: Comparison of the heave excitation force (a) Froude-Krylov component and (b) diffraction component, as computed by the new solver, with BEM solver Capytaine [3] for a submerged unit hemisphere .

The new solver demonstrates sufficient accuracy for practical applications, including early-stage design and sensitivity studies, in both diffraction and radiation problems, provided that irregular frequencies are not an issue. The deviation in the surge added mass and damping could be due to this issue and will be investigated further in future. Irregular frequencies occur when the numerical solution of the BIEs becomes unstable or non-unique

at certain discrete frequencies. These frequencies do not correspond to any physical phenomenon and can lead to inaccuracies in the computed hydrodynamic coefficients and its gradients. It is important to note that irregular frequencies are a well-known challenge [37] in existing BEM methods and will be addressed in future implementations of our solver.

In the next section, we discuss the differentiation of the new BEM solver and review concepts relevant to developing the differentiable code.

3. Gradient Computation in the BEM solver

A naive way to obtain the gradients of the computed hydrodynamic coefficients and excitation forces is to numerically approximate them using finite differences. However, this method involves solving the hydrodynamic problem multiple times—once for each design variable—resulting in a computational cost of $O(M \times N^3)$, where M is the number of design variables and N represents the discretized boundary elements in the BIEs. This makes the approach computationally expensive for high-dimensional problems.

A more efficient alternative is the adjoint-based method [1, 33], which decouples the cost of sensitivity computation from the number of design variables. While traditional solvers do not inherently include an adjoint solver, it can be derived as long as the BEM code provides the influence matrices and the boundary condition vectors. Adjoint solvers have been successfully applied in various fields, notably first by Jameson (1988) [27] for aircraft design optimization, borrowing techniques originally developed in optimal control theory [21]. The adjoint method has since become a cornerstone in high-dimensional design optimization [18].

3.1. Deriving the adjoint

Two primary approaches exist for formulating adjoints in the context of flow control and optimization (PDE-constrained optimization) problems: optimize-then-discretize (OtD) [22] and discretize-then-optimize (DtO). The OtD approach formulates the optimization problem (using the continuous equations) and derives its discrete form afterward, while the DtO approach first discretizes the governing equations and then derives the optimization problem, often resulting in different numerical behavior. Nadarajah and Jameson (2012) [42] review these approaches in the context of aerodynamic design problems and Bradley (2010) also discusses them in detail for general setting [10]. While both methods theoretically yield equivalent results,

practical considerations favor one over the other depending on the specific problem [10].

The OtD approach involves deriving the unconstrained optimization problem in its continuous form by formulating the Lagrangian:

$$\mathcal{L}(\theta, u, \lambda) = \mathcal{J}(\theta, u) + \lambda_l^T \mathcal{F}(\theta, u), \quad (34)$$

where x are the design variables, u are the state variables, $\mathcal{J}(x, u)$ is the objective function, $\mathcal{F}(x, u)$ represents the constraints (e.g., boundary conditions), and λ_l are the Lagrange multipliers used to enforce these constraints. The stationarity condition, $\nabla_u \mathcal{L} = 0$, provides the sensitivity of the boundary conditions, $F(x, u)$, with respect to the state variables u . Solving the resulting Karush-Kuhn-Tucker (KKT) conditions, discretized as a linear system, yields the solution to the adjoint boundary value problem [48]. Ragab (2012) [48] applied the OtD approach to free-surface flows, implementing a time-domain panel code for hydrodynamic ship design under forward speed in waves using translating and pulsating free surface Green’s function. The work formulated a wave resistance functional and a target pressure distribution for ship surfaces. They modified the panel code for the adjoint free-surface condition. However, the gradients derived in this approach were restricted to the specific objective function and may deviate from numerical results after discretization, as observed by Ragab (2012) who found up to 6% error in the gradients when compared with finite differences [48].

In contrast, this paper adopts the DtO approach, also known as the discrete adjoint method. This method is preferred for working with numerical solvers as it directly leverages the existing forward solver, ensuring exact gradients that are consistent with the numerical approximation of the discretized forward solve problem. This consistency between the computed function value and its gradients is crucial for reliable optimization, particularly when the objective function depends on these values.

For a discretized BIE system with influence matrices (operators) S and D , and b representing either the radiation or diffraction boundary condition for a specific degree of freedom, the state equation is

$$D(\theta)\phi - S(\theta)b(\theta) = 0, \quad (35)$$

where D and S are $n \times n$ asymmetric complex-valued dense square matrices.

The BIE constrained optimization problem is formulated as:

$$\begin{aligned} \min_{\theta, \phi} \quad & \mathcal{J}(\phi(\theta), \theta) \\ \text{subject to} \quad & D(\theta)\phi - S(\theta)b(\theta) = 0, \end{aligned} \quad (36)$$

where J is the objective function dependent on, vector of potential, $\vec{\phi}$ of each panel, and the design parameter, θ . The total derivative of \mathcal{J} with respect to θ is expressed as:

$$\frac{d\mathcal{J}}{d\theta} = \frac{\partial \mathcal{J}}{\partial \theta} + \left(\frac{\partial \mathcal{J}}{\partial \phi} \right)^T \frac{\partial \phi}{\partial \theta}. \quad (37)$$

To compute $\frac{\partial \phi}{\partial \theta}$, the linear system, Eq. 35 is perturbed as follows:

$$\frac{\partial(D\phi)}{\partial \theta} = \frac{\partial(Sb)}{\partial \theta} \quad (38)$$

$$\frac{\partial D}{\partial \theta} \phi + D \frac{\partial \phi}{\partial \theta} = \frac{\partial S}{\partial \theta} b + S \frac{\partial b}{\partial \theta} \quad (39)$$

$$D \frac{\partial \phi}{\partial \theta} = S \frac{\partial b}{\partial \theta} + b \frac{\partial S}{\partial \theta} - \phi \frac{\partial D}{\partial \theta} \quad (40)$$

$$\frac{\partial \phi}{\partial \theta} = D^{-1} \left(S \frac{\partial b}{\partial \theta} + b \frac{\partial S}{\partial \theta} - \phi \frac{\partial D}{\partial \theta} \right). \quad (41)$$

Substituting $\frac{\partial \phi}{\partial \theta}$ from Eq. 41 into Eq. 37 and grouping terms from left to right yields an additional system that can be used to solve for the adjoint variable λ :

$$\lambda^T = \frac{\partial J}{\partial \phi} D^{-1} \quad (42)$$

$$\lambda^T D = \frac{\partial J}{\partial \phi}. \quad (43)$$

The gradient of \mathcal{J} with respect to θ is then expressed as:

$$\frac{\partial \mathcal{J}}{\partial \theta} = \frac{\partial \mathcal{J}}{\partial \theta} + \lambda^T \left(\frac{\partial b}{\partial \theta} S + b \frac{\partial S}{\partial \theta} - \phi \frac{\partial D}{\partial \theta} \right). \quad (44)$$

Here, λ represents the adjoint variable that solves the adjoint linear system derived from the perturbed system. The gradient $\frac{\partial J}{\partial \theta}$ efficiently combines contributions from the boundary condition perturbation ($\frac{\partial b}{\partial \theta}$), matrix

perturbations $(\frac{\partial S}{\partial \theta}, \frac{\partial D}{\partial \theta})$, and the solution vector ϕ . This formulation avoids explicitly computing $\frac{\partial \phi}{\partial \theta}$, significantly reducing computational cost. In Eq. 37, $\frac{\partial \mathcal{J}}{\partial \theta} = 0$ in most applications, though for applications where there may be direct dependence (such as power per volume for a wave energy converter) it should be calculated. A similar derivation from the indirect BIE could also be performed to obtain the adjoint linear system.

To compute the required partial derivatives in the adjoint equation, methods such as finite differences, complex-step differentiation, symbolic differentiation, or AD can be employed. However, the accuracy and efficiency of gradient calculations vary with the chosen method. Finite difference may incur significant efficiency and truncation error issues. Complex-step differentiation avoids the truncation error however it requires the real and imaginary values be separable. This requirement may necessitate modifications to the algorithms and Green’s function used in computation [40]. Symbolic differentiation is exact but may be cumbersome to derive especially for computer programs. Out of these, AD is exact and scalable. In this context, differentiation is performed with respect to design variables such as the dimensions of floating bodies or the frequency of ocean waves.

As illustrated in the derivation above, the adjoint method reduces the number of the linear solves to just two, regardless of the number of the design variables [1]. This is equivalent to solving an additional adjoint boundary value problem for a single scalar function output. The computational cost, therefore, decreases from $O(M \times N^3)$ to $O(2 \times N^3)$, where N is the size of the dense, asymmetric matrices, and M is the number of design variables. Notably, the matrix required for the adjoint solve is the transpose of the matrix from the forward solve. This ensures that the matrix’s conditioning remains consistent, eliminating the need for higher precision in the Green’s function evaluations. However, this advantage may only apply to linear problems, as considered here.

3.2. Automating adjoint derivation

Manually deriving and assembling the adjoint equation can be complex and error-prone. For example, for the case of WEC design optimization the state equation may need to be solved multiple times, along with other linear systems like the equation of motion, before computing the objective function. A solver that abstracts this process can greatly enhance usability and streamline the design workflow. Reverse-mode AD is an effective alternative, assembling the partial derivatives required for the adjoint equation without

explicitly solving for adjoint variables. This approach works by propagating output perturbations backward through the computational chain. Unlike forward-mode AD, which traces input perturbations, reverse-mode AD is better suited for high-dimensional problems involving scalar objectives [13].

Relying on AD to differentiate through iterative solvers (common in BEM codes), however, can introduce inefficiencies and errors [20]. Instead, implicit differentiation is preferred. In implicit differentiation, for a system $F(x, u = 0)$, where u represents the solution and x is a design variable, gradients are obtained by solving a linear system at optimality $F(x, u(x)) = 0$. This bypasses the need for AD to “unroll” external iterative solver computations. We utilize libraries like `implicitAD` [46] and `Zygote` [26] to implicitly differentiate through the linear solver, allowing for efficient and automated adjoint setup within a single differentiable pipeline. This approach is solver-agnostic, meaning users can adopt any state-of-the-art linear system solver without modification, ensuring compatibility with a wide range of Julia-based scientific computing tools.

3.3. Regularization for differentiability

In our solver implementation, in addition to automating the adjoint of the linear solver, we differentiate the Green’s function, which presents challenges [34]. We apply AD to the midpoint quadrature method for integrating the Green’s function, noting that the accuracy of the results are influenced by the chosen integration method. This method is employed for constant panels, offering a balance between simplicity and computational efficiency. In the case of the Rankine and reflected Rankine terms, which are both of the form $\frac{1}{x}$, $x \rightarrow 0$ results in singularities. These are handled using a Rankine integration algorithm described by [45], with AD applied directly to compute derivatives of the integral efficiently. Similarly, in case of integration for the exact expression by Delhommeau [11], the differentiable HCubature method is implemented using `Integrals.jl` [53].

The frequency-dependent Green’s function depends on the horizontal (X) and vertical (Y) distances between panels relative to the free surface. However, spatial derivatives can become problematic when $d = \sqrt{h^2 + v^2} \rightarrow 0$, resulting in singularities. This numerical issue is mitigated by introducing a small regularization constant ($d + \epsilon$), ensuring gradient consistency with finite difference approximations. Regularization, relaxation, and reparameterization are common techniques in differentiable programming to stabilize gradients and ensure differentiability almost everywhere, making programs

robust and fully differentiable [8]. Since the Green’s function is an approximation, comparing its gradients with analytical ones is unnecessary; instead the gradients must remain consistent with the discretized forward solution to ensure the solver’s reliability and accuracy in design optimization studies.

3.4. Validation of the Green’s function gradients and radiation force derivatives

To validate the performance of the new solver, we evaluate its ability to compute the gradients of the Green’s function as well as the gradients of the radiation forces on a submerged unit hemisphere using the adjoint formulation with AD as compared to those obtained through the finite-difference method.

The wave component of the Green’s function (W in (21) which is frequency dependent) is an approximation that results in reduced accuracy compared to exact analytical values. Consequently, its gradients may not perfectly align with analytical results. In contrast, the gradients of the Rankine component (the first term in (21) which is frequency independent) can be directly validated against the analytical added mass of a submerged sphere in still water which does not include a free surface term. Specifically, the non-dimensional gradient for the added mass of a submerged sphere in surge in still water, given by

$$\frac{\partial A}{\partial r} = \frac{2\pi\rho r^2}{\frac{2}{3}\pi r^3\rho}, \quad (45)$$

is compared with the result obtained using AD, as illustrated in Figure 6. As we can see from the figure, the two methods align well, indicating the validity of the AD implementation in the new solver. The accuracy is expected to improve and converge toward analytical results with an increase in the number of panels and the use of an exact Green’s function expression.

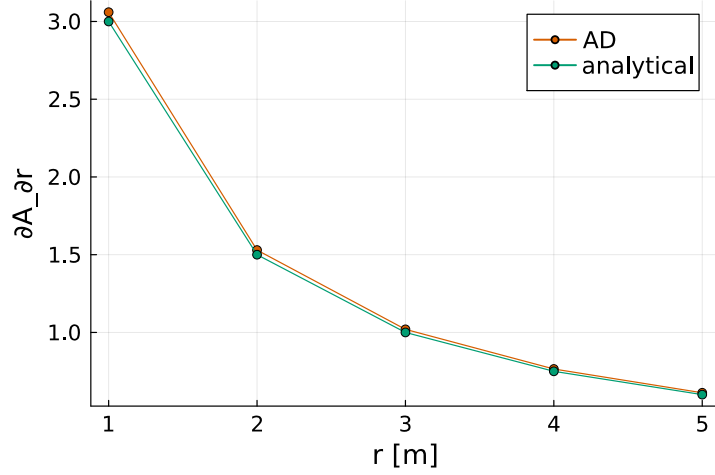


Figure 6: Comparison of the analytical and AD-computed gradients of added mass ($\frac{\partial A}{\partial r}$) for a surging hemisphere sphere in still water.

If we assume the body motion, ξ , takes the form:

$$\xi = \Re(\Xi e^{i\omega t}), \quad (46)$$

where Ξ is the complex body motion amplitude, then the radiation force described in Eq. (33) along a particular degree of freedom, i , can be simplified to

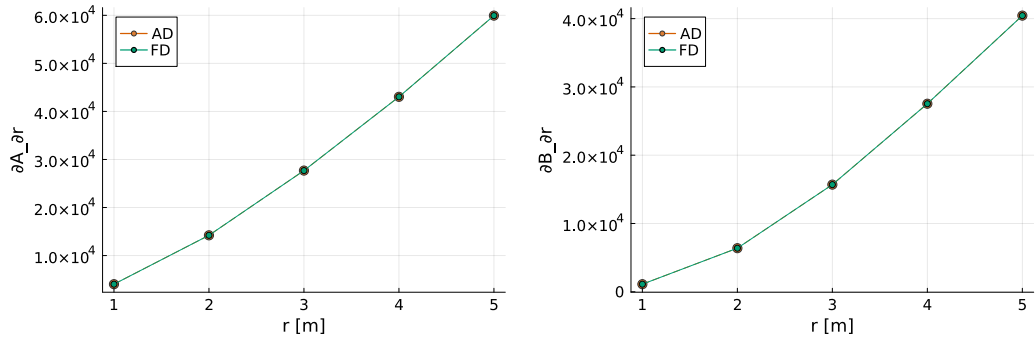
$$F_{R_i} = (-\omega^2 A_{ij} + i\omega B_{ij}) \cdot \xi_j. \quad (47)$$

In this context, let $f : \mathbb{R} \rightarrow \mathbb{C}$ map the dimension of the floating device (θ) to the radiation force. Then, f can be differentiated by treating it as $f : \mathbb{R} \rightarrow \mathbb{R}^2$, where the real and imaginary parts are differentiated independently. To compute the derivative of the radiation force F_{R_i} in the i -th degree of freedom with respect to the design variable θ , the real and imaginary components of the complex valued F_{R_i} are differentiated separately given in Eq. (47), as follows:

$$\frac{\partial F_{R_i}}{\partial \theta} = \frac{\partial \Re F_{R_i}}{\partial \theta} \cdot \xi_i + i \frac{\partial \Im F_{R_i}}{\partial \theta} \cdot \xi_i, \quad (48)$$

where $\Re F_{R_i}$ and $\Im F_{R_i}$ are the real and imaginary parts of the radiation force, respectively. By Eq. (47), this effectively amounts to differentiating each of the hydrodynamic coefficients (A_{ij} and B_{ij}) separately.

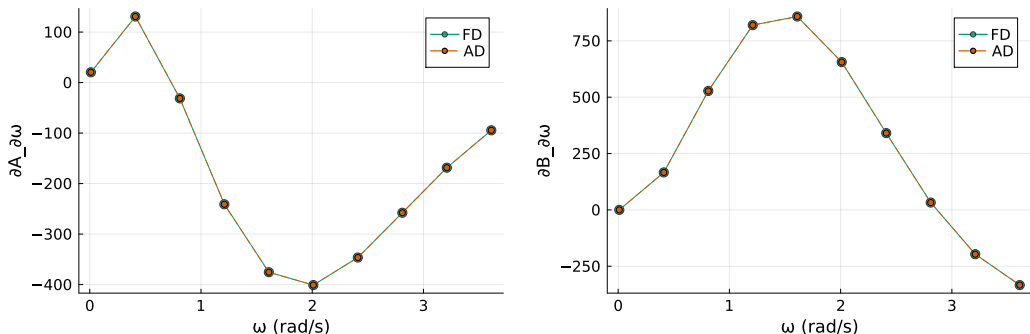
Figures 7 and 8 demonstrates that these real and imaginary gradients are exact when compared to those computed with finite differences, confirming their accuracy. In Figures 7a and 7b, we take the gradient with respect to the radius of the sphere, r , for a fixed incoming wave frequency $\omega = 1.03$ rad/s. We see that for both added mass and damping in heave, the gradient computed using AD with respect to radius for a range of hemisphere radii (1 m to 5 m) is nearly the same as that computed using finite difference, with an absolute error of $\leq 10^{-7}$ kg/m in added mass and $\leq 10^{-7}$ Ns/m in damping.



(a) Gradients for $\frac{\partial A}{\partial r}|_{\omega=1.03 \text{ rad/s}}$ using AD vs. finite difference. (b) Gradients for $\frac{\partial B}{\partial r}|_{\omega=1.03 \text{ rad/s}}$ using AD vs. finite difference.

Figure 7: Comparison of gradients computed by AD to those computed by finite difference (FD) for (a) heave added mass $\frac{\partial A}{\partial r}|_{\omega=1.03 \text{ rad/s}}$ (b) and heave damping $\frac{\partial B}{\partial r}|_{\omega=1.03 \text{ rad/s}}$.

Figures 8a and 8b show the gradient with respect to the incident wave frequency, ω , for a fixed sphere radius, $r = 1$ m. We see that for both added mass and damping in heave, the gradient computed using AD for a range of incident wave frequencies (0 rad/s to 3.6 rad/s) is nearly the same as that computed using finite difference, with an absolute error of $\leq 10^{-7}$ kg/m in added mass and $\leq 10^{-7}$ Ns/m in damping.



(a) Gradients for $\frac{\partial A}{\partial \omega}|_{r=1 \text{ m}}$ using AD vs. finite difference. (b) Gradients for $\frac{\partial B}{\partial \omega}|_{r=1 \text{ m}}$ using AD vs. finite difference.

Figure 8: Comparison of gradients computed by AD to those computed by finite difference (FD) for (a) heave added mass $\frac{\partial A}{\partial \omega}|_{r=1 \text{ m}}$ (b) and heave damping $\frac{\partial B}{\partial \omega}|_{r=1 \text{ m}}$.

Similarly, the new solver described in this paper can calculate the sensitivity in the case of either the direct and indirect BIE formulations, with a comparison for added mass and damping shown in Figure 16 in the appendix 12.

3.5. Solver computational speed

The new BEM solver takes approximately $11.676 \mu\text{s}$ and 486 memory allocations (17 KiB) to compute the Rankine term of the Green's function and 359.522 ns and 6 allocations (592 bytes) to compute the wave component of the Green's function per entry in the influence matrices. Gradient calculations with respect to radius and wave frequency are slower, taking about 1.6 s and 7647721 memory allocations (378.04 MiB) for a hemisphere of unit radius discretized into 18 panels. The allocations for reverse mode gradient calculation will be higher for complex geometries as they require more panels for reasonable accuracy. These measurements were obtained using Julia (version 1.10.5) running on a Linux platform with a single CPU thread and 256 GB memory.

The current implementation, while functional, is unoptimized for both coefficient and gradient calculations. Optimization efforts will be addressed in future work and are beyond the scope of this paper. Preliminary benchmarking indicates that, with optimizations of the forward solve (excluding differentiability), the performance can match that of the well-known BEM solver Capytaine [3]. Future optimization efforts will focus on ensuring that

differentiability is preserved, which is the goal of planned extensions to the current work presented in this paper.

In the next section, we delve into the implementation details of the solver, with a focus on ensuring efficient and accurate gradient propagation.

4. Implementation for differentiability

Traditional BEM solvers have not prioritized gradients, resulting in separate performant solvers and user-facing post-processing tools, complicating integration for modern differentiation-based methods. While existing tools like Tapenade [23], OpenMDAO [19], and other algorithmic differentiation frameworks [13] enable differentiability, they rely on operator overloading or program transformations. These approaches are suboptimal for BEM because forward solver routines—such as parallelization and memory management—directly impact adjoint solver efficiency [61]. Moreover, these methods often require significant modifications or entirely new solvers, as demonstrated by Rohrer et al. (2024) [49], whose workaround still faced memory limitations and inefficiencies for large-scale design tasks.

Challenges arise in practical applications, such as WEC layout optimization, where multiple adjoint calculations are required for each linear solve, involving multiple interacting bodies and degrees of freedom. Existing approaches often fix the mesh resolution and skip differentiating the influence matrix assembly process, limiting their ability to adapt to design changes. This fixed-matrix approach is not ideal for optimization tasks, as highlighted by Rohrer et al. (2024) [49], who emphasized the need for solvers inherently designed for differentiability.

The new BEM solver described in this paper addresses these limitations by making differentiability a core feature. It differentiates through the influence matrix assembly process, allowing gradients to be computed even as mesh resolution or design variables change. Unlike previous methods, it does not require fixed-size matrices, enabling flexibility for large-scale design optimization studies where an optimizer may make significant design adjustments. Although the current implementation is not yet fully optimized for memory efficiency, it is designed to overcome the constraints of earlier methods and provide high accuracy for realistic, complex design tasks.

The new BEM solver is implemented in the Julia programming language using a composition of pure, mutation-free functions. This approach allows

AD tools like Zygote to “natively” differentiate the source code via source-to-source AD. The implementation primarily rewrites the existing Fortran-based Green’s function used in Capytaine [3] and integral algorithms, adopting functional programming paradigms where appropriate. Zygote supports reverse-mode differentiation, which is crucial for design optimization, the primary motivation for this solver. Forward-mode differentiation, enabled by Julia’s dual number support, is also available and can be extended by implementing forward chain rules (as outlined in the following Subsection 4.2), though reverse-mode remains the focus for optimization tasks.

In the following subsection, we outline the methodology for enabling and propagating gradients throughout the BEM source code.

4.1. *Jacobian construction and Automatic Differentiation modes*

The required Jacobian ($J_{M \times N}$) of the M hydrodynamic coefficients with respect to N input parameters (e.g, wave frequency and body geometry variables) can be constructed either column-by-column or row-by-row. These two approaches correspond to two differentiation modes: Pushforward (forward mode) and pullback functions (backward mode, also called backpropagation) in Julia.

The pushforward operation computes the Jacobian-vector product (JVP), which propagates an input perturbation (∂x) through the function to compute the resulting perturbation in the output (∂y):

$$\partial y = J \cdot \partial x. \tag{49}$$

This approach is useful for building the Jacobian column-by-column, as it calculates the effect of a small change in each input on the outputs.

The pullback operation computes the vector-Jacobian product (VJP) by introducing a perturbation in the output space (∂y) and propagating it back through the function to determine the impact on the input space (∂x):

$$\partial x^\top = \partial y^\top \cdot J. \tag{50}$$

This method is ideal for building the Jacobian row-by-row as it computes how small changes in each output affect all inputs simultaneously. It is particularly efficient when dealing with optimization objectives or constraints where only a few outputs matter.

4.2. Custom Chain Rules for Automatic Differentiation

The Julia library Zygote is used to perform these operations by perturbing the Julia code directly. For code that is not written in Julia or contains unsupported constructs, however, we implement custom gradient propagation rules using the ChainRulesCore.jl package [62]. For example, our new solver leverages the external libraries Capytaine [3] for mesh pre-processing, which is not differentiable. We therefore use ChainRulesCore.jl to specify custom chain rules to propagate gradients through the AD computational graph. Future implementations of our new BEM solver will aim to replace external libraries like Capytaine with fully differentiable mesh pre-processing code.

Mesh pre-processing involves generating the mesh vertices and panel properties for the BEM solver. For example, a meshing function $f_{\text{mesh}}(r) \rightarrow \text{vertices}$ calculates the mesh vertices for a sphere given the radius r . The Jacobian of this function is then computed using finite differences, and augmented with a custom reverse-mode rule for AD in Zygote, enabling gradient propagation. The reverse-mode differentiation rule for Zygote computes the vector-Jacobian product:

$$\frac{\partial f_{\text{mesh}}}{\partial r}^\top \cdot \delta y, \quad (51)$$

where δy is the gradient propagated back from the output of BEM solver to the meshing function.

This approach can be extended to other mesh panel properties required for BEM coefficient calculations. Although finite differences are used for mesh pre-processing, this is computationally acceptable because the operations are not as cost-intensive as linear solves. By defining custom AD rules, the solver ensures compatibility with differentiable pipelines while maintaining accuracy in numerical gradients.

Algorithm 1 illustrates the implementation process for the custom reverse-mode differentiation rule for mesh computations used in our new BEM solver.

4.3. Applications and Future Directions

The custom AD rules developed here are not limited to mesh pre-processing but can be extended to any external CAD geometry tools, enabling a fully differentiable pipeline for calculating hydrodynamics coefficients. This approach

Algorithm 1 Custom reverse-mode differentiation rule (rrule) for mesh computations $f_{\text{mesh}}(x)$

```

1: Input:  $x$  (input vector),  $dy$  (perturbation from the output)
2: Output:  $y$  (function output),  $dx$  (gradient w.r.t.  $x$ )
3: Define  $f_{\text{mesh}}(x)$  external operation:
4: function RRULE( $f_{\text{mesh}}, x$ )
5:    $y \leftarrow f_{\text{mesh}}(x)$  ▷ Compute the primal value
6:   function PULLBACK( $dy$ )
7:      $df \leftarrow \text{NoTangent}()$  ▷ No tangent contribution
8:      $dx \leftarrow \frac{\partial f_{\text{mesh}}}{\partial r}^\top \cdot dy$  ▷ Compute Vector-Jacobian product
9:     return ( $df, dx$ )
10:  end function
11:  return ( $y, \text{pullback}$ )
12: end function

```

can also integrate post-processing operations and non-computationally intensive tasks in hydrodynamic analysis. Non-computationally intensive tasks refer to those that do not scale with the number of input variables, as opposed to operations that scale polynomially like linear solvers, which are more resource-intensive.

Reverse-mode AD, while powerful, requires more memory than the forward mode because it caches all intermediates values during the forward solve for use in backpropagation. Future iterations of this solver will explore performance optimizations such as checkpointing and the incorporation of analytical derivatives to reduce memory usage and enhance efficiency [20]. Additionally, other AD engines available in Julia will be evaluated to identify opportunities for improved performance and scalability.

In the following sections, we conduct two case studies to demonstrate some of the capabilities of the new solver.

5. Case study I: Sensitivity of hydrodynamic coefficients for two identical floating spheres

Exploring the hydrodynamic interactions between closely spaced floating bodies can provide valuable insights for designing systems that leverage constructive wave interaction effects for power generation [31, 56]. Analyzing these interactions can be used to identify a separation distance at which

simpler models, such as the plane wave approximation (PWA) [55], can be applied to significantly reduce the computational costs associated with computing the hydrodynamic response of floating bodies in a given wave environment [65]. Currently, this distance is considered to be approximately five times the radius of the floating body, beyond which simpler hydrodynamic coefficients approximations can be used with minimal accuracy loss [55].

For WECs, understanding how variables such as body dimensions, inter-body spacing, and wave climate influence energy absorption is essential for designing robust and cost-effective array layouts. These factors play a critical role in optimizing power production and ensuring the effectiveness of energy farms [9].

In this case study, we examine two identical heaving spheres (point absorbers) (Figure 9) using the fully differentiable BEM solver described earlier. This solver is extended to compute two-body hydrodynamic interactions. We calculate the exact local sensitivities of each sphere’s hydrodynamic coefficients (added mass and damping) relative to the influence on other sphere. These sensitivities are evaluated with respect to their separation distance (x) and the frequency of the wave environment (ω) for a fixed-size spheres of radius r . The dimensionless parameters ($kr, \frac{x}{r}$) are varied to calculate the gradients providing insights into hydrodynamic interactions between floating bodies.

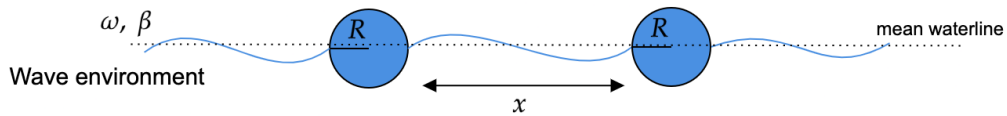


Figure 9: Schematic of a pair of identical floating spheres.

The coupled and symmetric added mass matrix (A)

$$\begin{bmatrix} A_{11} & A_{12} \\ A_{21} & A_{22} \end{bmatrix}, \quad (52)$$

and the damping matrix (B)

$$\begin{bmatrix} B_{11} & B_{12} \\ B_{21} & B_{22} \end{bmatrix} \quad (53)$$

are computed for the two heaving spheres. Sensitivities are analyzed to understand interactions, with gradients computed using AD in the new solver via the Green's function approximation by Wu et al. (2017) [63].

5.1. Sensitivity Results and Observations

Figures 10 and 11 illustrate the sensitivities of the coupled added mass (A_{12}) and coupled damping (B_{12}), respectively, with respect to the sphere radius, (r), swept over the separation distance ratio ($\frac{x}{r}$) and wavenumber (kr). Figure 10 shows that the sensitivity of A_{12} varies from normalized values 0 to 1 (corresponding to 420.4 kg/m to -750 kg/m originally) showing strong spatial dependency. Negative-to-positive gradient transitions highlight regions where increasing ω significantly alters the coupled effect, likely due to wave interference.

Similarly, Figure 11 shows that the damping sensitivities with respect to radius range from from normalized values 0 to 1 (corresponding to 2148.89 Ns/m to -1291.43 Ns/m originally). The damping coefficients exhibit regions of increasing or decreasing sensitivity depending on the distance and sphere size. Both added mass and damping sensitivities demonstrate non-uniform variations with separation distance and frequency, underscoring the importance of layout optimization for instance in WEC arrays.

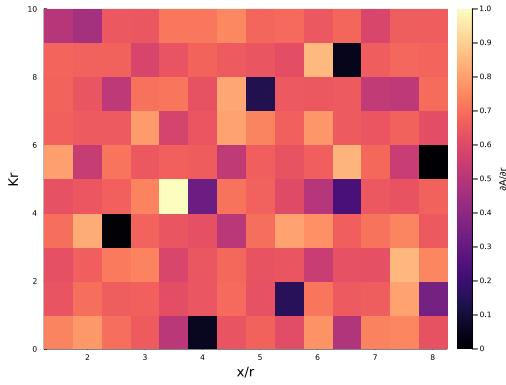


Figure 10: Sensitivity of added mass (A_{12}) with respect to radius (r) for unit spheres: $\frac{\partial A_{12}}{\partial r} \Big|_{r=1 \text{ m}}$

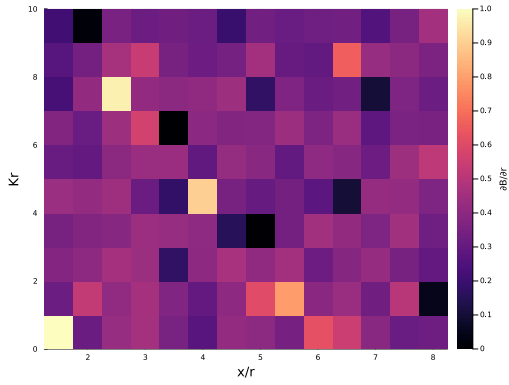


Figure 11: Sensitivity of damping (B_{12}) with respect to radius (r) for unit spheres: $\frac{\partial B_{12}}{\partial r} \Big|_{r=1 \text{ m}}$

The sensitivity of added mass (A_{11}) and damping (A_{11}) of unit hemisphere ($r_1 = 1m$) at $\omega = 1.03 \text{ rad/s}$ with respect to the dimension of a nearby sphere (r_2) can be calculated to establish PWA heuristics [55], enabling the application of simplified interaction models at larger distances.

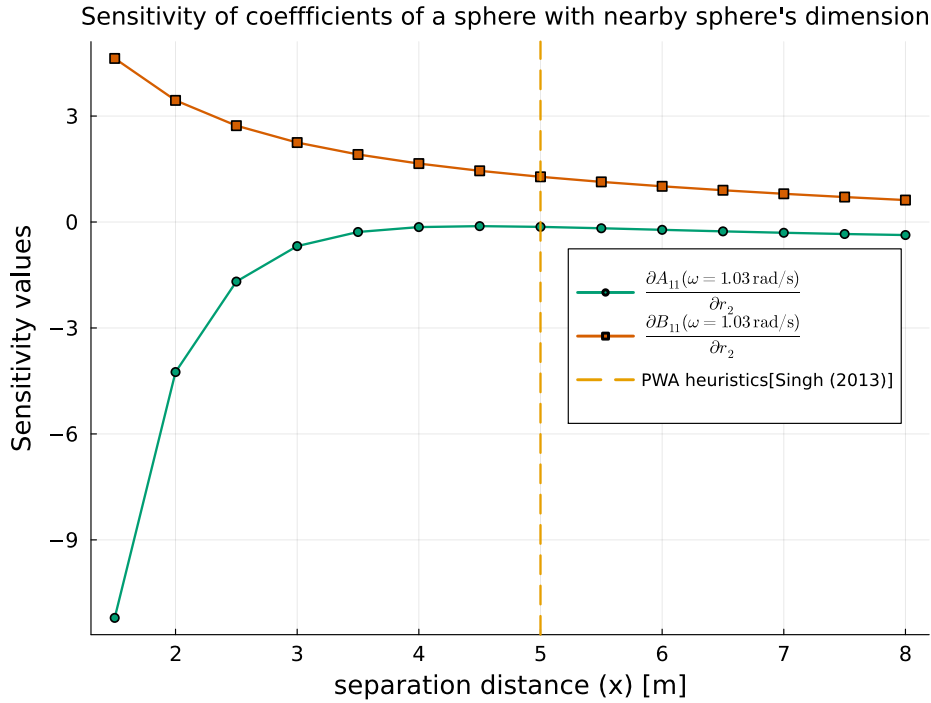


Figure 12: Sensitivity of sphere 1’s added mass and damping coefficients with respect to the dimension of sphere 2 as well as PWA heuristics for simplified interaction modeling [55].

Figure 12 illustrates $\frac{\partial A_{11}}{\partial r_2}$ and $\frac{\partial B_{11}}{\partial r_2}$ approaching zero as the separation distance increases, indicating that sphere 1’s coefficients become independent of sphere 2’s dimension. This result aligns with expectations, as the added mass and damping of a body are influenced by fluid flow around the body, which depends on the geometry of nearby obstacles such as the sea bed or other floating bodies. For the infinite-depth case considered in this solver, the sea bed is not a nearby obstacle. Similar numerical studies can be conducted for various geometries before implementing simplified models at large distances. For instance, Singh et al. (2013)[55] used a cutoff distance of five times the characteristic dimension before assuming plane wave interactions. From Figure 12 it seems that this is a good rule of thumb. It is also noteworthy that the rates at which the sensitivities of added mass and damping decrease to zero differ, reflecting the distinct hydrodynamic influences on these coefficients.

5.2. Implications for Design and Optimization

These results reveal critical “transition regions” in sensitivities, emphasizing the need to account for realistic wave climates (encompassing all relevant ω) in layout optimization studies. For instance, certain changes in sphere dimensions can offset sensitivity changes due to increased separation distances. This interplay can be exploited in optimization tasks to achieve desired performance metrics, such as maximizing energy absorption.

The spatial sensitivities computed using the approximation by Wu et al. [63] align within 2% of those derived from exact Delhommeau expressions [11] as shown in appendix 12, Figure 15, validating the solver’s accuracy for design optimization tasks when using the faster Green’s function approximation. These exact sensitivities are essential for guiding experimental setups and improving the practicality of large-scale numerical design optimization.

6. Case study II: Optimization of mechanical power from pair of point absorbers

In this section, we demonstrate the capabilities of the new BEM solver by optimizing the mechanical power for two identical point absorbers WECs for a fixed wave frequency $\omega = 1.03$ rad/s as shown in Figure 13. The objective is to find the optimal dimensions and the distance between the absorbers to maximize mechanical power. While realistic wave spectra, waveroses, and larger WEC arrays would typically be considered in practical applications, this case study focuses on showcasing the solver’s functionality; hence a smaller scope is considered.

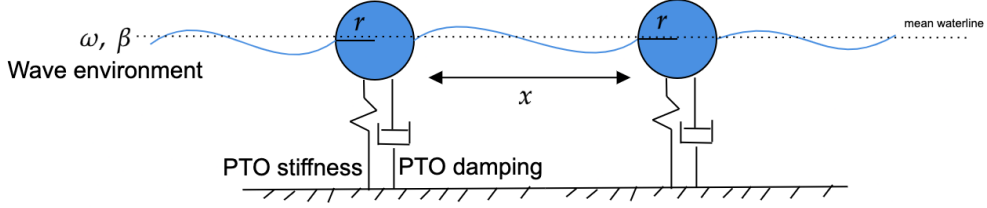


Figure 13: Pair of point absorbers separated by distance x

6.1. Methodology

To propagate the gradients efficiently, the dynamics, control systems, and power calculations for the WECs were implemented in Julia, with hydrostatics made differentiable using custom chain rules as described in Subsection 4.2. A resistive controller is used, setting the PTO stiffness to zero ($k_i = 0$), and the PTO damping coefficient is set to be equal to the hydrodynamic damping coefficient $\vec{d} = \text{diag}(\mathbf{B})$ for each sphere.

For linear PTO devices, the time-averaged power, P , for each WEC is given by:

$$P_i = \frac{1}{2} d_i |j\omega \mathbb{E}_i(i\omega)|^2 \quad (54)$$

where $\mathbb{E}_i(i\omega)$ is the complex amplitude of heave motion. The coupled dynamics of the system are solved using the frequency-domain linear equation:

$$\vec{\mathbb{E}}(i\omega) = [-\omega^2(\mathbf{M} + \mathbf{A}) - i\omega(\mathbf{B} + \text{diag}(\vec{d})) + \mathbf{C} + \text{diag}(\vec{k})]^{-1} \vec{\mathbb{F}}(i\omega), \quad (55)$$

where \mathbf{A} is the 2×2 added mass matrix, \mathbf{B} is the 2×2 hydrodynamic damping matrix, $\vec{\mathbb{F}}(j\omega)$ is the 1×2 wave excitation force vector, \mathbf{C} is the 2×2 hydrostatic stiffness matrix, \mathbf{M} is the 2×2 diagonal mass matrix, $\text{diag}(\vec{d})$ is a diagonal matrix of the PTO damping coefficients for unit wave amplitude. The hydrodynamic coefficients and wave exciting force (\mathbf{A} , \mathbf{B} , $\vec{\mathbb{F}}(i\omega)$) are computed using the new BEM solver, while \mathbf{C} is obtained from Capytaine

[3] and integrated into the differentiable pipeline via custom chain rules as described in Subsection 4.2. Note that, \mathbf{C} is not the function of frequency ω .

With this solver, for this case study, no manual adjoint derivation is required for either the linear systems (integral equation) or the equations of motion, as the solver handles these processes automatically. This greatly simplifies implementation, enabling efficient handling of downstream calculations. For instance, in scenarios where WECs interact across multiple degrees of freedom, linear systems described in Eq. 35 must be solved for each degree of freedom. To illustrate the solver’s scalability, consider a WEC farm with N interacting bodies in one degree of freedom and W wave frequencies (ω) in a spectrum. This setup would require solving $W \times N^2$ radiation problems and $W \times N$ diffraction problems. The automated handling provided by our new BEM solver makes such complex scenarios more manageable and computationally feasible.

The optimization problem for this case study is formulated as follows:

$$\text{Minimize } \mathcal{J}(\hat{\theta}) = \frac{\sum_i P_i}{\frac{4}{3}\pi r^3} \quad (56)$$

$$\text{by varying } \hat{\theta} = [r, x] \quad (57)$$

$$\text{subject to } d_s > 0 \quad (58)$$

$$\text{while solving } \begin{bmatrix} D(\omega)\phi - S(\omega)b \\ -\omega^2(\mathbf{M} + \mathbf{A}) - i\omega(\mathbf{B} + \text{diag}(\mathbf{B})) + \mathbf{C})^{-1}\mathbf{E}(i\omega) - \mathbf{F}(i\omega) \end{bmatrix} = \begin{bmatrix} 0 \\ 0 \end{bmatrix} \quad (59)$$

where \mathcal{J} is the total mechanical power per unit volume, $\hat{\theta}$ is vector of design variables, r is the radius of the point absorber, x is the separation distance, S and D are influence matrices, and b is the boundary condition defined in (12) and (13).

6.2. Results and Discussion

The accuracy of the gradients of the objective function with respect to the design variables computed by the new solver was verified against finite difference results. Table 2 shows excellent agreement between the methods:

Design Variable	Finite Difference Gradient	AD Gradient	Absolute Error
radius (1 m)	170.437647446	170.43764737445	$\leq 10^{-9}$
separation distance (5 m)	-0.2635335396	-0.2635335398	$\leq 10^{-9}$

Table 2: Comparison of gradients: finite difference vs. AD

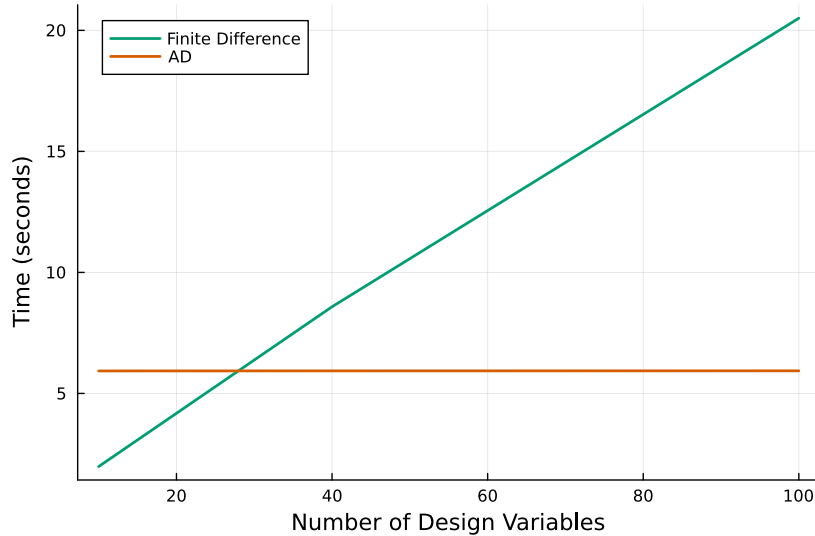


Figure 14: Comparison of computation times: finite difference vs. AD as the number of design variables increase

Table 2 also shows that the sensitivity of the power calculation for two point absorbers depends more on their body dimension than their separation distance at the chosen ocean wave frequency ($\omega = 1.03$ rad/s).

To see how our new solver scales with additional design variables, the optimization problem was modified to include some “dummy” design variables which have no effect on the objective function value. Figure 14 compares the computation times for gradients obtained via numerical finite differences and AD in our new solver. It demonstrates that as the number of design variables increases, the time required for a single gradient evaluation using finite difference grows significantly. In contrast, AD maintains a constant computation time regardless of the number of design variables. Current AD implementation has higher computation times (y -intercept for AD) due to the unoptimized reverse-mode differentiation and it increases with mesh resolution. Future iterations of the solver are expected to reduce these times substantially through performance optimizations.

The optimization was carried out using the Limited-memory Broyden-Fletcher-Goldfarb-Shanno (L-BFGS) algorithm via Optim.jl [41]. The nominal and optimal design variables as well as the optimal objective function value are summarized in Table 3. The optimizer converged in three iterations

and 857 seconds, selecting point absorbers with the smallest allowed radius and maximum separation distance when using AD.

Variable	Bounds	Nominal Value	Optimal Value
Radius (r [m])	[1.0, 4.0]	2.0	1.0
Separation Distance (x [m])	[1.0, 4.0]	2.0	3.9
Optimal Objective Function Value		24.48 W/m ³	

Table 3: Summary of Optimization Results

This case study demonstrates the scalability of AD for high-dimensional problems, as the cost of gradient computation remains constant regardless of the number of design variables. Although this case study only considers two design variables, real-world WEC layout optimization typically involves numerous interacting bodies across a range of wave frequencies within a spectrum [59]. Importantly, AD’s computational efficiency ensures that gradient calculations are equally cost-effective for both small-scale and large-scale optimization tasks, making it well-suited for complex, high-dimensional scenarios.

The current example, with just two variables, is not ideal for showcasing the full potential of reverse-mode AD but serves as a simplified demonstration. Reverse-mode AD is particularly advantageous for high-dimensional problems, such as the design optimization of multiple interacting bodies in wind-wave layout configurations. For realistic applications, detailed optimization would require greater computational resources, but this solver is expected to incur significantly lower costs compared to traditional methods like finite differences or heuristic optimization.

Future work will focus on performance optimization of the solver, including modular code enhancements to accommodate larger arrays of interacting bodies and more complex wave spectra. Additionally, a comprehensive comparison between heuristic and gradient-based optimization approaches will be conducted to further evaluate the solver’s capabilities and efficiency.

7. Conclusion

In this work, we developed and implemented a novel fully differentiable BEM solver capable of accurately computing hydrodynamic coefficients and their gradient calculations using AD. The solver incorporates both exact and surrogate Green’s functions and supports direct and indirect boundary integral formulations. By leveraging reverse-mode AD within Julia, the solver achieves precise and scalable gradient calculations, overcoming limitations in traditional BEM solvers that often requires researchers to rely on finite differences or heuristic methods when used for optimization.

Through rigorous numerical experiments, we validated the solver’s accuracy against analytical benchmarks and demonstrated its practical utility in two case studies. The first case study analyzed hydrodynamic interactions between two identical floating spheres, revealing critical insights into the sensitivity of coupled hydrodynamic coefficients to design and environmental parameters. The second case study applied the solver to optimize the mechanical power production of a WEC array, illustrating its potential for system-level design optimization. Both studies confirmed the solver’s ability to handle complex, large-scale optimization tasks with high efficiency.

This work highlights the potential of integrating differentiable programming into marine hydrodynamics. By eliminating the need for manual adjoint derivation and enabling seamless gradient propagation, the proposed solver simplifies workflows and extends the capabilities of traditional BEM approaches. This advancement not only accelerates adjoint based optimization and local uncertainty quantification but also opens avenues for integrating machine learning and data-driven approaches in offshore engineering.

Looking forward, the solver provides a framework for tackling real-world challenges such as WEC farm layout optimization, floating wind turbine design, and other applications requiring precise sensitivity analysis. As the offshore industry shifts toward more complex and integrated design frameworks, the adoption of differentiable tools like this solver will be crucial for advancing engineering innovation and operational efficiency.

8. Future Work

Future work will focus on optimizing the solver’s performance for both forward solves and backward gradient propagation. Key improvements also include implementing parallel processing and integrating matrix-vector acceleration techniques, such as H-matrices, while ensuring these algorithms

remain differentiable for fast and efficient BEM code. Empirical evidence suggest that manually defining derivatives in Julia’s AD systems, where feasible, can significantly accelerate the overall AD process. These enhancements are crucial for achieving a scalable and performant BEM approach.

Another priority for future work is leveraging Julia’s GPU capabilities to accelerate both the forward and backward solves. Given BEM’s is inherently data-parallel nature, it is well-suited for the GPU computations, provided the kernel functions are efficiently implemented for GPU devices. This could lead to substantial speedups in large-scale simulations.

In addition to performance improvements, we aim to extend the solver’s application to large-scale systems engineering challenges, such as design optimization and uncertainty quantification in wave-structure interaction analyses. Specific applications include optimizing WEC array layouts and analyzing wave-induced loads on offshore structures in infinite depth. The extension of this solver for finite depth scenario will also be considered in future iterations.

Finally, we plan to continue developing the package to support the mesh pre-processing and hydrostatics components in Julia (which currently relies externally on Capytaine), improving the modularity to handle multiple bodies, ensuring a fully integrated and differentiable workflow.

The code for this paper is available open-source with release tag v0.1.0

<https://github.com/symbiotic-engineering/MarineHydro.jl>

9. CRediT authorship contribution statement

Kapil Khanal: Conceptualization, Methodology, Software, Formal analysis, Investigation, Data Curation, Original Draft, Review & Editing, Visualization. **Dr. Carlos A. Michelén Ströfer:** Conceptualization, Methodology, Review & Editing, Funding acquisition. **Dr. Matthieu Ancellin:** Methodology, Software, Review & Editing. **Dr. Maha N Haji:** Conceptualization, Resources, Supervision, Writing - Review & Editing, Funding acquisition.

10. Acknowledgement

Authors would like to thank Prof. David Bindel, Olivia Vitale, Collin Treachy and Julia discourse members for their valuable feedback and discussion on the simulation, analysis and code derivation in this manuscript. This

work was supported in part by the Seedling and Sapling program by the US Department of Energy.

11. Funding Statement

Sandia National Laboratories is a multi-mission laboratory managed and operated by National Technology & Engineering Solutions of Sandia, LLC (NTESS), a wholly owned subsidiary of Honeywell International Inc., for the U.S. Department of Energy's National Nuclear Security Administration (DOE/NNSA) under contract DE-NA0003525. This written work is authored by an employee of NTESS. The employee, not NTESS, owns the right, title and interest in and to the written work and is responsible for its contents. Any subjective views or opinions that might be expressed in the written work do not necessarily represent the views of the U.S. Government. The publisher acknowledges that the U.S. Government retains a non-exclusive, paid-up, irrevocable, world-wide license to publish or reproduce the published form of this written work or allow others to do so, for U.S. Government purposes. The DOE will provide public access to results of federally sponsored research in accordance with the DOE Public Access Plan.

12. Appendix

Comparison of Wu and Delhommeau's sensitivities with respect to the separation distance.

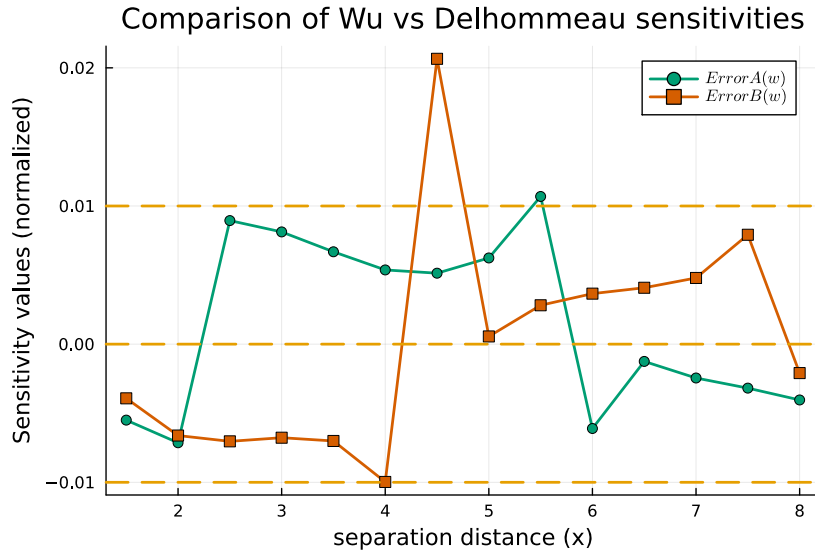


Figure 15: Error in added mass and damping sensitivities using Wu vs Delhommeau's exact Green's function at $\omega = 1.03$ rad/s

Comparison of hydrodynamic sensitivities computed via direct and indirect BIE formulation using surrogate Green's function .

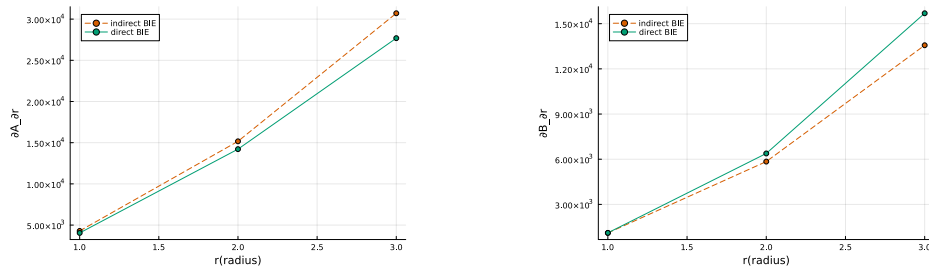


Figure 16: Comparison of gradients computed by AD for direct and indirect BIE formulations for (a) heave added mass $\frac{\partial A}{\partial \omega}|_{r=1 \text{ m}}$ (b) and heave damping $\frac{\partial B}{\partial \omega}|_{r=1 \text{ m}}$.

References

- [1] Allaire, G., 2015. A review of adjoint methods for sensitivity analysis, uncertainty quantification and optimization in numerical codes. Ing. Automob. 836.

- [2] Ancellin, M., 2024. On the accuracy of linear boundary-element-method sea-keeping codes, in: 19e Journées de l’Hydrodynamique, École Centrale de Nantes, Nantes, France.
- [3] Ancellin, M., Dias, F., 2019. Capytaine: a Python-based linear potential flow solver. *Journal of Open Source Software* 4, 1341. URL: <https://doi.org/10.21105/joss.01341>, doi:10.21105/joss.01341.
- [4] Ashuri, T., Zaaier, M., Martins, J., van Bussel, G., van Kuik, G., 2014. Multidisciplinary design optimization of offshore wind turbines for minimum leveled cost of energy. *Renewable Energy* 68, 893–905.
- [5] Babarit, A., Delhommeau, G., 2015. Theoretical and numerical aspects of the open source BEM solver NEMOH, in: *Proceedings of the 11th European Wave and Tidal Energy Conference (EWTEC2015)*, Nantes, France.
- [6] Bartholomew-Biggs, M., Brown, S., Christianson, B., Dixon, L., 2000. Automatic differentiation of algorithms. *Journal of Computational and Applied Mathematics* 124, 171–190.
- [7] Bigoni, D., 2015. *Uncertainty Quantification with Applications to Engineering Problems*. Phd thesis. Technical University of Denmark.
- [8] Blondel, M., Roulet, V., 2024. The elements of differentiable programming. URL: <https://arxiv.org/abs/2403.14606>, arXiv:2403.14606.
- [9] Borgarino, B., Babarit, A., Ferrant, P., 2012. Impact of wave interactions effects on energy absorption in large arrays of wave energy converters. *Ocean Engineering* 41, 79–88.
- [10] Bradley, A.M., 2010. *Pde-constrained optimization and the adjoint method*. URL: https://cs.stanford.edu/~ambrad/adjoint_tutorial.pdf. original November 16, 2010, revised July 7, 2024.
- [11] Delhommeau, G., 1987. *Problèmes de diffraction-radiation et de résistance des vagues : étude théorique et résolution numérique par la méthode des singularités*. Phd thesis. École Nationale Supérieure de Mécanique de Nantes. Nantes, France.

- [12] Dou, S., Pegalajar-Jurado, A., Wang, S., Bredmose, H., Stolpe, M., 2020. Optimization of floating wind turbine support structures using frequency-domain analysis and analytical gradients. *Journal of Physics: Conference Series* 1618, 042028.
- [13] Elliott, C., 2018. The simple essence of automatic differentiation. *Proc. ACM Program. Lang.* 2. URL: <https://doi.org/10.1145/3236765>, doi:10.1145/3236765.
- [14] Falnes, J., 2002. *Ocean Waves and Oscillating Systems: Linear Interactions Including Wave-Energy Extraction*. Cambridge University Press.
- [15] Folley, M., et al., 2016. Wave energy converter modelling techniques based on linear hydrodynamic theory, in: Folley, M. (Ed.), *Numerical Modelling of Wave Energy Converters*. Elsevier. chapter 1, pp. 11–65.
- [16] Forrester, A.I., Keane, A.J., 2009. Recent advances in surrogate-based optimization. *Progress in Aerospace Sciences* 45, 50–79.
- [17] Gaul, L., Koegl, M., Wagner, M., 2003. *Boundary Element Methods for Engineers and Scientists: An Introductory Course With Advanced Topics*. volume 57. doi:10.1115/1.1849172.
- [18] Giles, M.B., Pierce, N.A., 2000. An introduction to the adjoint approach to design. *Flow, Turbulence and Combustion* 65, 393–415. Received 13 December 1999; accepted in revised form 2 February 2000.
- [19] Gray, J.S., Hwang, J.T., Martins, J.R., Moore, K.T., Naylor, B.A., 2019. Openmdao: An open-source framework for multidisciplinary design, analysis, and optimization. *Structural and Multidisciplinary Optimization* 59, 1075–1104.
- [20] Griewank, A., Walther, A., 2008. *Evaluating Derivatives*. Second ed., Society for Industrial and Applied Mathematics.
- [21] Grund, F., 1985. Pironneau, o., optimal shape design for elliptic systems. berlin-heidelberg-new york-tokyo, springer-verlag 1984. xii, 168 s., dm 80,—. us \$ 29.90. isbn 3-540-12069-6 (springer series in computational physics). *ZAMM - Journal of Applied Mathematics and Mechanics / Zeitschrift für Angewandte Mathematik und Mechanik* 65, 523–523.

- [22] Gunzburger, M.D., 1987. Perspectives in flow control and optimization. URL: <https://api.semanticscholar.org/CorpusID:121957251>.
- [23] Hascoet, L., Pascual, V., 2013. The tapenade automatic differentiation tool: Principles, model, and specification. *ACM Trans. Math. Softw.* 39. URL: <https://doi.org/10.1145/2450153.2450158>, doi:10.1145/2450153.2450158.
- [24] Ho Choi, J., Man Kwak, B., 1990. A unified approach for adjoint and direct method in shape design sensitivity analysis using boundary integral formulation. *Engineering Analysis with Boundary Elements* 7, 39–45.
- [25] Hulme, A., 1982. The wave forces acting on a floating hemisphere undergoing forced periodic oscillations. *Journal of Fluid Mechanics* 121, 443. doi:10.1017/s0022112082001980.
- [26] Innes, M., 2018. Don't unroll adjoint: Differentiating ssa-form programs. CoRR abs/1810.07951. URL: <http://arxiv.org/abs/1810.07951>, arXiv:1810.07951.
- [27] Jameson, A., 1988. Aerodynamic design via control theory. *Journal of Scientific Computing* 3, 233–260. URL: <https://doi.org/10.1007/BF01061285>, doi:10.1007/BF01061285.
- [28] John, F., 1950. On the motion of floating bodies ii. simple harmonic motions. *Communications on Pure and Applied Mathematics* 3. URL: <https://onlinelibrary.wiley.com/doi/abs/10.1002/cpa.3160030106>, doi:<https://doi.org/10.1002/cpa.3160030106>, arXiv:<https://onlinelibrary.wiley.com/doi/pdf/10.1002/cpa.3160030106>.
- [29] Kenway, G.K., Mader, C.A., He, P., Martins, J.R., 2019. Effective adjoint approaches for computational fluid dynamics. *Progress in Aerospace Sciences* 110, 100542.
- [30] Koh, C.S., Hahn, S.Y., Chung, T.K., Jung, H.K., 1992. A sensitivity analysis using boundary element method for shape optimization of electromagnetic devices. *IEEE transactions on magnetics* 28, 1577–1580.
- [31] Konispoliatis, D., Mavrakos, S., 2016. Hydrodynamic analysis of an array of interacting free-floating oscillating water column (owcs) devices. *Ocean Engineering* 111, 179–197.

- [32] Lee, C.H., Newman, J., Kim, M.H., Yue, D., 1991. The computation of second-order wave loads, in: Proceedings of the OMAE '91 Conference, Stavanger, Norway.
- [33] Lettermann, L., Jurado, A., Betz, T., Wörgötter, F., Herzog, S., 2024. Tutorial: a beginner's guide to building a representative model of dynamical systems using the adjoint method. *Communications Physics* 7, 128.
- [34] Liang, H., Shao, Y., Chen, J., 2021. Higher-order derivatives of the green function in hyper-singular integral equations. *European Journal of Mechanics - B/Fluids* 86, 223–230.
- [35] Liang, H., Wu, H., Noblesse, F., 2018. Validation of a global approximation for wave diffraction-radiation in deep water. *Applied Ocean Research* 74, 80–86. doi:10.1016/j.apor.2018.02.025.
- [36] Liu, Y., 2019. Hams: A frequency-domain preprocessor for wave-structure interactions—theory, development, and application. *Journal of Marine Science and Engineering* 7.
- [37] Liu, Y., Falzarano, J.M., 2017. Irregular frequency removal methods: theory and applications in hydrodynamics. *Marine Systems & Ocean Technology* 12, 49–64.
- [38] Mackay, E., 2019. Consistent expressions for the free-surface green function in finite water depth. *Applied Ocean Research* 93, 101965. URL: <https://www.sciencedirect.com/science/article/pii/S0141118719304456>, doi:<https://doi.org/10.1016/j.apor.2019.101965>.
- [39] Martins, J., Kennedy, G., 2021. Enabling large-scale multi-disciplinary design optimization through adjoint sensitivity analysis. *Structural and Multidisciplinary Optimization* 64, 2959–2974. URL: <https://doi.org/10.1007/s00158-021-03067-y>, doi:10.1007/s00158-021-03067-y.
- [40] Martins, J.R.R.A., Ning, A., 2022. *Engineering Design Optimization*. Cambridge University Press.

- [41] Mogensen, P.K., White, J.M., Riseth, A.N., Holy, T., Lubin, M., von Salis, C., Noack, A., Levitt, A., Ortner, C., Legat, B., Johnson, B., Rackauckas, C., Yu, Y., Carlsson, K., Lin, D., Strouwen, A., Grawitter, J., Arakaki, T., Pasquier, B., Covert, T.R., Rock, R., Creel, M., cossio, Regier, J., Kuhn, B., Stukalov, A., Williams, A., Sato, K., 2024. Julianlsolvers/optim.jl: v1.10.0. URL: <https://doi.org/10.5281/zenodo.14092087>, doi:10.5281/zenodo.14092087.
- [42] Nadarajah, S., Jameson, A., . A comparison of the continuous and discrete adjoint approach to automatic aerodynamic optimization.
- [43] Newman, J., 1984. Approximations for the Bessel and Struve functions. *Mathematics of Computation* 43, 551–556.
- [44] Newman, J.N., 1985. Algorithms for the free-surface Green function. *Journal of Engineering Mathematics* 19.
- [45] Newman, J.N., 1986. Distributions of sources and normal dipoles over a quadrilateral panel. *Journal of Engineering Mathematics* 20, 113–126.
- [46] Ning, A., McDonnell, T., 2023. Automating steady and unsteady adjoints: Efficiently utilizing implicit and algorithmic differentiation. arXiv preprint arXiv:2306.15243 , 12URL: <https://doi.org/10.48550/arXiv.2306.15243>. 12 pages, 3 figures.
- [47] Patryniak, K., Collu, M., Coraddu, A., 2022. Multidisciplinary design analysis and optimisation frameworks for floating offshore wind turbines: State of the art. *Ocean Engineering* 251, 111002.
- [48] Ragab, S.A., 2004. Shape optimization of surface ships in potential flow using an adjoint formulation. *AIAA Journal* 42, 296–304.
- [49] Rohrer, P.J., Bachynski-Polić, E.E., 2024. Analytical gradients of first-order diffraction and radiation forces for design optimization of floating structures. *Applied Ocean Research* 152, 104198.
- [50] Ruehl, K., Leon, J., Michelen, C., Topper, M., Tom, N., Baca, E., Ogden, D., 2023. Next-Generation Marine Energy Software Needs Assessment. Technical Report. Sandia National Laboratories and National Renewable Energy Laboratory. URL: <https://www.nrel.gov/docs/fy23osti/84936.pdf>. sAND2023-03906R, NREL/TP-5700-84936.

- [51] Rumelhart, D.E., Hinton, G.E., Williams, R.J., 1986. Learning representations by back-propagating errors. *Nature* 323, 533–536.
- [52] Sauter, S.A., Schwab, C., 2011. *Boundary Element Methods*. Springer Berlin Heidelberg, Berlin, Heidelberg. pp. 183–287.
- [53] SciML, 2025. *Integrals.jl: Numerical integration tools in julia*. URL: <https://github.com/SciML/Integrals.jl>. accessed: 2025-01-08.
- [54] Silva, O.M., Serafim, L.P., Mareze, P.H., Fonseca, W.D., Cardoso, E.L., 2023. Discrete approach for shape optimization of 2d time-harmonic acoustic radiation problems solved by bem using the fully-analytical adjoint method. *Engineering Analysis with Boundary Elements* 156, 548–571.
- [55] Singh, J., Babarit, A., 2013. Hydrodynamic interactions in multiple body array: A simple and fast approach coupling boundary element method and plane wave approximation, in: *Proceedings of the International Conference on Offshore Mechanics and Arctic Engineering*. URL: <https://doi.org/10.1115/OMAE2013-10541>, doi:10.1115/OMAE2013-10541.
- [56] Singh, J., Babarit, A., 2014. A fast approach coupling boundary element method and plane wave approximation for wave interaction analysis in sparse arrays of wave energy converters. *Ocean Engineering* 85, 12–20. URL: <https://www.sciencedirect.com/science/article/pii/S0029801814001589>, doi:<https://doi.org/10.1016/j.oceaneng.2014.04.019>.
- [57] Sobol', I.M., 2001. Global sensitivity indices for nonlinear mathematical models and their monte carlo estimates. *Mathematics and Computers in Simulation* 55, 271–280.
- [58] Takahashi, T., Sato, D., Isakari, H., Matsumoto, T., 2022. A shape optimisation with the isogeometric boundary element method and adjoint variable method for the three-dimensional helmholtz equation. *Computer-Aided Design* 142, 103126.
- [59] Teixeira-Duarte, F., Clemente, D., Giannini, G., Rosa-Santos, P., Taveira-Pinto, F., 2022. Review on layout optimization strategies of

- offshore parks for wave energy converters. *Renewable and Sustainable Energy Reviews* 163, 112513.
- [60] Tortorelli, D.A., Michaleris, P., 1994. Design sensitivity analysis: Overview and review. *Inverse Problems in Engineering* 1, 71–105.
- [61] Towara, M., Naumann, U., 2013. A discrete adjoint model for openfoam. *Procedia Computer Science* 18, 429–438. doi:10.1016/j.procs.2013.05.206.
- [62] White, F., Abbott, M., Zgubic, M., Revels, J., Robinson, N., Arslan, A., Widmann, D., Schaub, S.D., Ma, Y., Tebbutt, W., Axen, S., Rackauckas, C., Vertechi, P., BSnelling, Fischer, K., st, Horikawa, Y., Cottier, B., Ranocha, H., Monticone, P., 2024. Juliadiff/chainrulescore.jl: v1.25.0. URL: <https://doi.org/10.5281/zenodo.13776884>, doi:10.5281/zenodo.13776884.
- [63] Wu, H., Zhang, C., Zhu, Y., Li, W., Wan, D., Noblesse, F., 2017. A global approximation to the green function for diffraction radiation of water waves. *European Journal of Mechanics -B/Fluids* 65, 54–64. URL: <https://www.sciencedirect.com/science/article/pii/S0997754616305064>, doi:<https://doi.org/10.1016/j.euromechflu.2017.02.008>.
- [64] Xie, C., Choi, Y., Rongere, F., Clement, A.H., Delhommeau, G., Babarit, A., 2018. Comparison of existing methods for the calculation of the infinite water depth free-surface green function for the wave-structure interaction problem. *Applied Ocean Research* 81, 150–163. URL: <https://www.sciencedirect.com/science/article/pii/S0141118718304917>, doi:<https://doi.org/10.1016/j.apor.2018.10.007>.
- [65] Zhang, D., Yuan, Z.M., Du, J., Li, H., 2022. Hydrodynamic modelling of large arrays of modularized floating structures with independent oscillations. *Applied Ocean Research* 129, 103371.
- [66] Zhang, J., Taflanidis, A.A., Scruggs, J.T., 2020. Surrogate modeling of hydrodynamic forces between multiple floating bodies through a hierarchical interaction decomposition. *Journal of Computational Physics* 408, 109298.

- [67] Zheng, S., et al., 2024. Recent advances in marine hydrodynamics. *Physics of Fluids* 36, 070402. URL: <https://doi.org/10.1063/5.0214089>, doi:10.1063/5.0214089.